LETTER

https://doi.org/10.1038/s41586-018-0601-5

Exciton–polariton topological insulator

S. Klembt[1,5]*, T. H. Harder[1,5], O. A. Egorov[1], K. Winkler[1], R. Ge[2], M. A. Bandres[3], M. Emmerling[1], L. Worschech[1], T. C. H. Liew[2], M. Segev[3], C. Schneider[1] & S. Höfling[1,4]*

Topological insulators—materials that are insulating in the bulk but allow electrons to flow on their surface—are striking examples of materials in which topological invariants are manifested in robustness against perturbations such as defects and disorder[1]. Their most prominent feature is the emergence of edge states at the boundary between areas with different topological properties. The observable physical effect is unidirectional robust transport of these edge states. Topological insulators were originally observed in the integer quantum Hall effect[2] (in which conductance is quantized in a strong magnetic field) and subsequently suggested[3–5] and observed[6] to exist without a magnetic field, by virtue of other effects such as strong spin–orbit interaction. These were systems of correlated electrons. During the past decade, the concepts of topological physics have been introduced into other fields, including microwaves[7,8], photonic systems[9,10], cold atoms[11,12], acoustics[13,14] and even mechanics[15]. Recently, topological insulators were suggested to be possible in exciton-polariton systems[16–18] organized as honeycomb (graphene-like) lattices, under the influence of a magnetic field. Exciton-polaritons are part-light, part-matter quasiparticles that emerge from strong coupling of quantum-well excitons and cavity photons[19]. Accordingly, the predicted topological effects differ from all those demonstrated thus far. Here we demonstrate experimentally an exciton-polariton topological insulator. Our lattice of coupled semiconductor microcavities is excited non-resonantly by a laser, and an applied magnetic field leads to the unidirectional flow of a polariton wavepacket around the edge of the array. This chiral edge mode is populated by a polariton condensation mechanism. We use scanning imaging techniques in real space and Fourier space to measure photoluminescence and thus visualize the mode as it propagates. We demonstrate that the topological edge mode goes around defects, and that its propagation direction can be reversed by inverting the applied magnetic field. Our exciton-polariton topological insulator paves the way for topological phenomena that involve light–matter interaction, amplification and the interaction of exciton-polaritons as a nonlinear many-body system.

Microcavity exciton-polaritons (sometimes simply called polaritons hereafter) are composite bosons originating from the strong coupling of quantum-well excitons to microcavity photons. While the excitonic fraction provides strong nonlinearity, the photonic part results in a low effective mass, allowing the formation of a Bose–Einstein condensate that is dissipative in nature and can be driven by a laser beam[20]. Polaritons have thus been described as "quantum fluids of light"[21]. For the epitaxially well-controlled III–V semiconductor system, several techniques are available to micropattern cavities and thus precisely engineer the potential landscapes of polaritons[22]. With recent advances bringing topological effects into the realms of photonics and polaritonics[7–10,23], several ways to realize topological edge propagation with polaritons have been suggested[16–18], with honeycomb geometries ('artificial graphene'[24]) being of particular interest to realize a Chern band insulator with Chern number $C=2$ (refs [17,18]). Polariton honeycomb lattices have been found to support Dirac-cone dispersions[25] as well as edge modes[26] inherited from their graphene origin[27,28]. Here, we take the next step and create a topological Chern insulator in a symbiotic part-light, part-matter system: the system of exciton-polaritons. Our experiments are based on the proposals[17,18] of a honeycomb potential landscape for exciton-polaritons, with its time-reversal symmetry broken by an applied magnetic field.

Let us first introduce the underlying physics and show its features in numerical simulations with a realistic set of sample parameters. The experiments display reliable condensation of polaritons in the vicinity of the Dirac cones and the creation of topological edge modes by applying a magnetic field. Hence, we consider the injection of polaritons into the topological gap and focus on the inherent properties of the chiral edge modes.

A general schematic of the experiment is presented in Fig. 1a. Figure 1b, c depicts the calculated dispersion relation of the honeycomb structure in the direction $\Gamma \rightarrow K$, connecting two Dirac cones (K and K′), without and with an applied magnetic field, respectively. The effective spin–orbit coupling of polaritons, induced by transverse electric/transverse magnetic (TE–TM) mode splitting, breaks the polarization-related symmetry, and thus each Dirac point transforms into four inverted parabolas[18]. Whereas the spin–orbit interaction is extremely small in real graphene[29], 'polariton graphene' offers the possibility of making the effective spin–orbit coupling large enough to open a sizable gap in a magnetic field. Without a magnetic field, the two central parabolas touch each other at the Dirac cones of the underlying honeycomb lattice (Fig. 1b). The degeneracy between the states in the crossing points can be lifted in the presence of a magnetic field and a finite Zeeman splitting. As a consequence, an energy gap forms near the Dirac cones (Fig. 1c). It is worth mentioning that the Dirac cones K and K′ are not equivalent. At the K (K′) point, the 'valence' band is formed from the B (A) pillars, and the 'conduction' band is formed from the A (B) pillars[18]. The reversed order of the bands in the basis of the sublattices signifies that the gap is topologically non-trivial[1].

The interplay of an external magnetic field and the effective spin–orbit coupling (TE–TM mode splitting) results in non-zero Berry connections around the K and K′ points, contributing to the total band Chern number $C=\pm 2$ (refs [17,18]). As a consequence, the honeycomb structure supports one-way propagating edge states for the energies within the topological gap. Figure 1c demonstrates the results of a band structure calculation combined with the dispersion of the edge states localized at the zigzag edge of the honeycomb structure. The propagation direction of these edge states is related to the direction of the external magnetic field: the polariton edge current is either left-moving (L, yellow) or right-moving (R, red), depicted in Fig. 1a, depending on the sign of the magnetic field. Figure 1e depicts the corresponding calculated edge mode.

To illustrate the existence and robustness of the topologically protected one-way edge states, we simulate the evolution of a wavepacket excited locally (Fig. 1f, g; red circle) at the zigzag edge of the honeycomb structure. Figure 1f, g shows that the launched wavepacket starts

[1]Technische Physik and Wilhelm-Conrad-Röntgen-Research Center for Complex Material Systems, Universität Würzburg, Würzburg, Germany. [2]Division of Physics and Applied Physics, School of Physical and Mathematical Sciences, Nanyang Technological University, Singapore, Singapore. [3]Physics Department and Solid State Institute, Technion, Haifa, Israel. [4]SUPA, School of Physics and Astronomy, University of St Andrews, St Andrews, UK. [5]These authors contributed equally: S. Klembt, T. H. Harder. *e-mail: sebastian.klembt@physik.uni-wuerzburg.de; sven.hoefling@physik.uni-wuerzburg.de

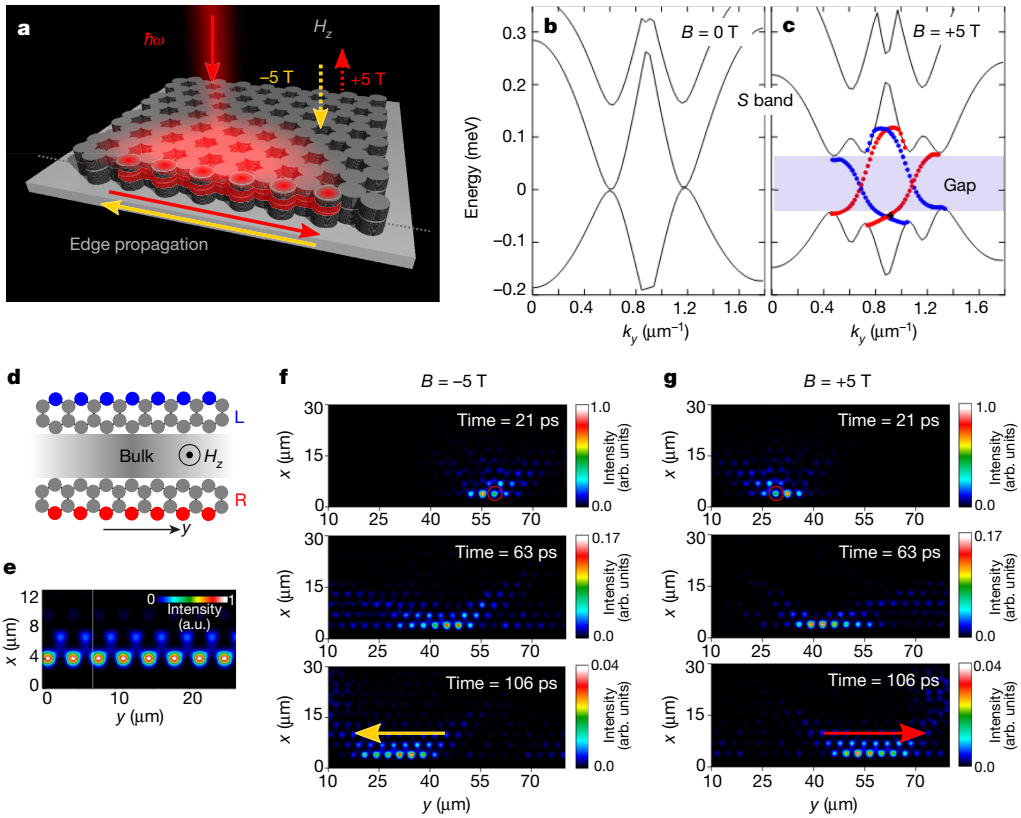

Fig. 1 | Experimental scheme, calculated band structure and simulated dynamics of the topological polariton edge modes. a, Schematic of the non-resonant laser excitation of left-moving (yellow) and right-moving (red) chiral topological polariton edge modes in a magnetic field H_z. **b**, **c**, Trivial and topological band structures of the polariton honeycomb lattice for zero Zeeman splitting (**b**) and with Zeeman splitting of $\Delta_{\mathrm{eff}} = 0.2$ meV, induced by the external magnetic field (**c**). One-way topological edge modes are represented by red (right-moving) and blue (left-moving) data points within the topological gap. **d**, **e**, Schematic (**d**) and calculated (**e**) intensity profiles of the edge modes. **f**, **g**, Calculated propagation dynamics of edge modes injected coherently (red circles) into the topological gap: left-moving time sequence (yellow) for negative Zeeman splitting $\Delta_{\mathrm{B}} = -0.8$ meV (**f**) and right-moving propagation (red) for positive Zeeman splitting $\Delta_{\mathrm{B}} = +0.8$ meV (**g**). arb. units, arbitrary units.

to propagate left or right along the edge, depending on the polarity of the magnetic field, whereas in the absence of magnetic field, the launched wavepacket remains at the excitation point. Note that the overall intensity decreases with propagation, as the model takes into account a realistic polariton lifetime of about 35 ps (see Methods for details). The simulations reveal that the chiral edge mode is topologically protected, as it propagates along the 90° corner and is able to pass a point-like defect without scattering (see Methods).

Having established the features that we expect to observe in an exciton-polariton topological insulator, we describe the experimental platform. To realize a honeycomb potential lattice, we fabricate a planar microcavity containing three $In_{0.04}Ga_{0.96}As$ quantum wells in a λ-cavity, sandwiched between two GaAs/AlGaAs distributed Bragg reflectors (DBRs) (Fig. 2a). Subsequently, we use electron beam lithography to define the honeycomb lattice, using micropillars with a diameter of $d = 2.0$ μm and a pillar-to-pillar overlap of $v = a/d = 0.85$, where a denotes the centre-to-centre distance between neighbouring pillars. Finally, the upper DBR is etched in such a way that only two DBR pairs of the top DBR remain, so as not to damage the active quantum-well region (Fig. 2b, c) (see Methods). When these sites are arranged in a two-dimensional lattice, the discrete pillar modes hybridize because of their proximity to one another and form a polaritonic band structure. The honeycomb lattice is characterized by a two-element base in real space (Fig. 2d) and two non-equivalent K and K′ points supporting Dirac cones in the first Brillouin zone (Fig. 2e), as well known from graphene. Figure 2f depicts characterization of the polariton honeycomb lattice in the linear regime, using non-resonant laser excitation. The Fourier-space energy-resolved photoluminescence of the investigated lattice is imaged in the k_y direction and scanned in the k_x direction. The blue data points are fitted to the measured dispersions, accurately revealing the six Dirac cones at the K and K′ points. The results of the corresponding tight-binding model (see Methods for details) are plotted in red and brown, agreeing well with the experimental data.

Next, we describe the experiments conducted on the honeycomb exciton-polariton lattice under an external magnetic field, aiming to find topologically non-trivial edge states. To be able to observe a bandgap that opens at the Dirac points, the Zeeman splitting and the TE–TM splitting at the Dirac points need to be sufficiently large compared with the photoluminescence linewidth. This implies that the polaritons need to have a sufficient excitonic part. Therefore, we select a lattice at a moderate negative exciton-to-photon detuning of $\delta = -11.5$ meV as summarized in the Methods.

To assess the size of the bandgap, we apply polarization-resolved spectroscopy, making use of a $\lambda/4$ polarization series at an external magnetic field of $B = 0$ T and 5 T. At an external magnetic field of $B = +5$ T, the Hopfield coefficients at the Dirac points yield a photonic fraction of $|C|^2 = 0.96$ and an excitonic fraction of $|X|^2 = 0.04$. Furthermore, the TE–TM splitting at the wavevector of the Dirac point (that is, $|k_{\mathrm{D}}| \approx 0.77\pi/a$) can be estimated to be 400 μeV for the photons, resulting in an effective TE–TM splitting for the exciton-polaritons of about 384 μeV ($\beta_{\mathrm{eff}} \approx 263$ μeV μm^2; see Methods). The Zeeman splitting of the excitonic mode is determined to be about 540 μeV, leading to an effective Zeeman splitting of $\Delta_{\mathrm{eff}} \approx 22$ μeV at the Dirac point (see Methods). As the TE–TM splitting is considerably larger than the Zeeman splitting in the lattice studied here, the experimentally determined bandgap that opens because of the magnetic field is $\Delta_{\mathrm{g}} = 108 \pm 32$ μeV with $\Delta_{\mathrm{eff}} < \Delta_{\mathrm{g}} < \beta_{\mathrm{eff}}$, which, as we show later, is

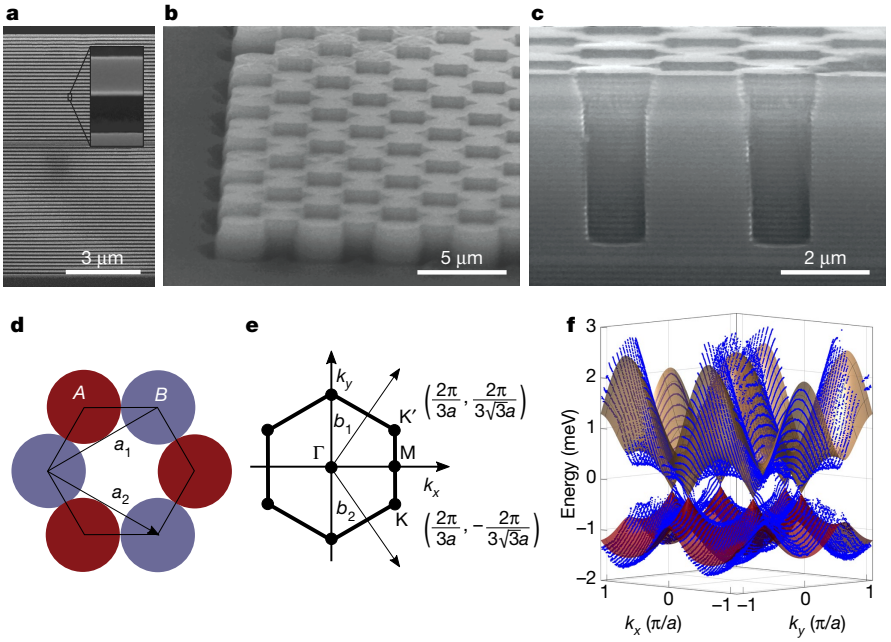

Fig. 2 | Lattice device layout and geometry. a–c, Scanning electron microscope images of the processed polariton honeycomb lattice. **a**, Cleaved cross-section of the microcavity before processing. **b**, Tilted view of the half-etched honeycomb lattice for pillars with a diameter of $d = 2.0\,\mu$m and an overlap $v = a/d = 0.85$. **c**, Cleaved cross-section after etching, showing that only the top DBR has been etched. **d**, Real-space honeycomb unit cell with two-element basis. **e**, First Brillouin zone of the honeycomb lattice, featuring the two non-equivalent K and K′ points. **f**, Measured Fourier-space energy-resolved photoluminescence of the investigated lattice. The blue data points are fitted to the measured dispersions, agreeing well with a tight-binding model (red and brown), accurately revealing the six Dirac cones at the K and K′ points.

reasonable for observing the topological features of our lattice and compares well with a gap size of about 100 μeV found for realistic system parameters[17].

After having established that a bandgap opens at the Dirac points under the influence of an external magnetic field, we use non-resonant excitation, under conditions allowing for polariton condensation into a chiral edge state within this bandgap. Scans of the photoluminescence signal in real space as well as Fourier space are performed on the polariton lattice at external magnetic fields of $B = -5$ T, 0 T and +5 T. The sample is excited on the zigzag edge by a pulsed and chopped laser beam with a diameter of 40 μm at 792 nm wavelength, tuned to the first stopband minimum (see Fig. 1a). In Fig. 3a and b, the linear polariton dispersion in the K′ → Γ → K direction at $B = 0$ T and at $B = +5$ T is displayed. The Dirac-cone dispersion is clearly visible ($P \approx 0.1$ mW). At a threshold power of $P_{th} = 1.8$ mW, we observe a nonlinear increase of the output power as well as a sudden decrease in linewidth (see Methods for details), establishing that a polariton condensate has formed at the K and K′ points at around $k_y \approx \pm 0.77\pi/a$, as displayed in Fig. 3c. We now perform mode tomography, scanning the real-space (x, y) landscape and measuring the photoluminescence energy E_{PL}. Figure 3d shows the spectrum of a line perpendicular to the zigzag edge, taken at the position indicated by the solid white line in Fig. 3g. The dashed white line depicts the edge of the sample. Besides an *S*-band condensate throughout the excited structure at $E_S = 1.4674$ eV, we observe an edge mode: a region of high intensity residing only at the outermost row of lattice sites spatially and spectrally at an energy of 1.4678 eV (white ellipse in Fig. 3d)—the expected topological bandgap.

Figure 3e shows the intensity pattern integrated over the energetic range of the trivial *S*-band mode centred at 1.4674 eV. Clearly, the condensate is relatively homogeneous over a large fraction of the lattice. The white overlaid lattice geometry and the microscopy image insets illustrate the position of the edge of the sample. Now, by changing the energy of the mode tomography to an energy $E_{edge} = 1.4678$ eV, within the topological gap (under a magnetic field of +5 T), the existence of edge states becomes unequivocal (at $x \approx 8\,\mu$m in Fig. 3g). The photoluminescence at this energy originates predominantly from the outermost row of lattice sites, with almost no emission detected from the bulk of the lattice. The mode is in excellent agreement with the Bloch-mode calculations in Fig. 1e–g. In addition, the theoretical description within a Ginzburg–Landau-based model confirms that polariton condensation into the edge mode occurs (see Methods for details).

We now move on to study the robustness of the topological edge state. We do so by installing an artificial defect into the lattice at $y = 15\,\mu$m (white circle in Fig. 3e–g). The defect is formed by leaving one of the sites on the zigzag edge of the honeycomb lattice unoccupied (see Methods). Normally, such a strong defect would cause scattering into the bulk, but here (see Fig. 3f, g) such scattering is suppressed, indicating that the transport of the topological edge state is immune to such defects. In addition, we perform mode tomography using non-resonant excitation with a large spot at the corner position of the sample. When plotting the energy of the topological edge mode $E_{edge} = 1.4678$ eV in Fig. 3f, one clearly observes that the mode extends around the corner from the zigzag into the armchair configuration, without any sign of backscattering or bulk scattering. The measurements at $B = -5$ T show very similar behaviour, but the transport is in the opposite direction. When the magnetic field is absent ($B = 0$ T), the edge mode vanishes completely (see Methods for details). The observation of the edge mode around the corner and especially its existence at the armchair edge, where topologically trivial honeycomb lattices do not have edge modes[9,27], prove that the edge mode we observe is indeed topological and is endowed with topological protection.

For further insight into the nature of these edge states, we analyse hyperspectral images ((k_x, k_y) versus E_{PL}) to identify the dominant propagation direction, with and without magnetic field. The results are displayed in Fig. 4. While in real space the modes can be clearly separated in energy, the integration over Fourier space results in the topological edge mode and the trivial bulk modes overlying one another. Figure 4a, b depicts the integrated intensities of the full *S*-band condensate (1.467–1.468 eV), including the energies associated with the edge state, for experiments at $B = +5$ T and −5 T, respectively. To analyse the directionality of polariton transport, the maximum peak intensities at the two maxima at $k_x \approx 0$ and $k_y \approx \pm 0.77\pi/a$ are extracted by identifying the central pixel of the peak and averaging the intensity

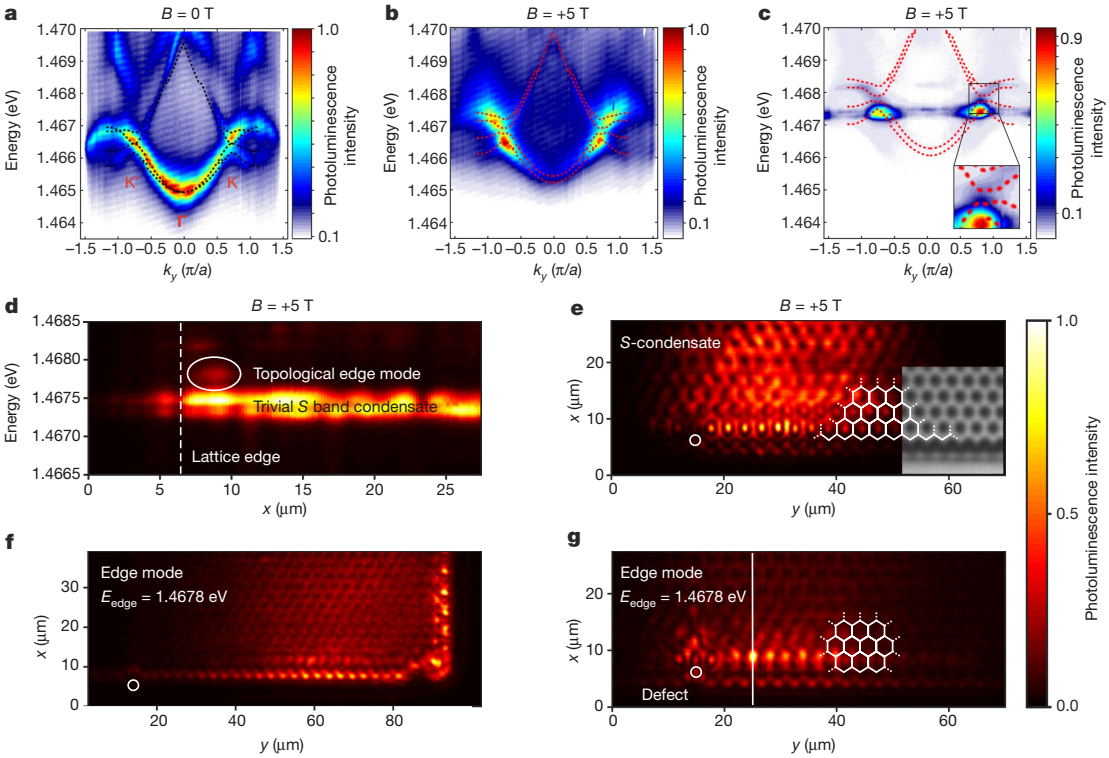

Fig. 3 | Photoluminescence measurements of a polariton condensate in a topological edge mode. a, Polariton dispersion along the K′ → Γ → K direction at $B = 0$ T compared with the calculated Bloch-mode model (black dots). **b**, **c**, Equivalent dispersions at $B = +5$ T, below (**b**) and above (**c**) the threshold $P_{th} = 1.8$ mW, where condensation into the K and K′ points of the *S* band is observed. Bloch-mode calculations (red dots) show a distinct gap. **d**, Real-space spectrum in the *x* direction along the straight white line in **g**. The *x* axis in **d**, **e** and **g** is the same. A trivial *S*-band condensate throughout the structure and a mode ($E = 1.4678$ eV) well separated from the bulk, located at the zigzag edge (dashed white line), are observed. **e**, Mode tomography displaying a homogeneous trivial *S*-band condensate ($E_S = 1.4673$–1.4675 eV) within the pump spot diameter of 40 μm. The inset shows a microscopy image of the structure. **f**, **g**, Mode tomography of the topological edge mode ($E_{edge} = 1.4678$ eV) at the corner position of the sample (**f**) and at the same position as in **e** (**g**). The mode is well located at the zigzag edge and clearly extends around the corner to the armchair configuration.

of a region of 3 × 3 pixels centred around this position. The vertical axis of Fig. 4c shows the ratio of the luminescence travelling in one direction ($+k_y$) to that in the opposite direction ($-k_y$). Deviation of this quantity from unity is an essential characteristic of a chiral state, and an opposite deviation should appear for opposite applied magnetic field. The corresponding intensity ratios are plotted in blue and show a clear directionality when an external magnetic field is applied. The transport changes its predominant direction along the edge when the direction of the magnetic field is inverted. This observation supports the interpretation of the edge-states being a result of a topologically non-trivial bandgap, with the edge mode contributing to the chirality along the edge. Reversing the magnetic field reverses the slope of the dispersion

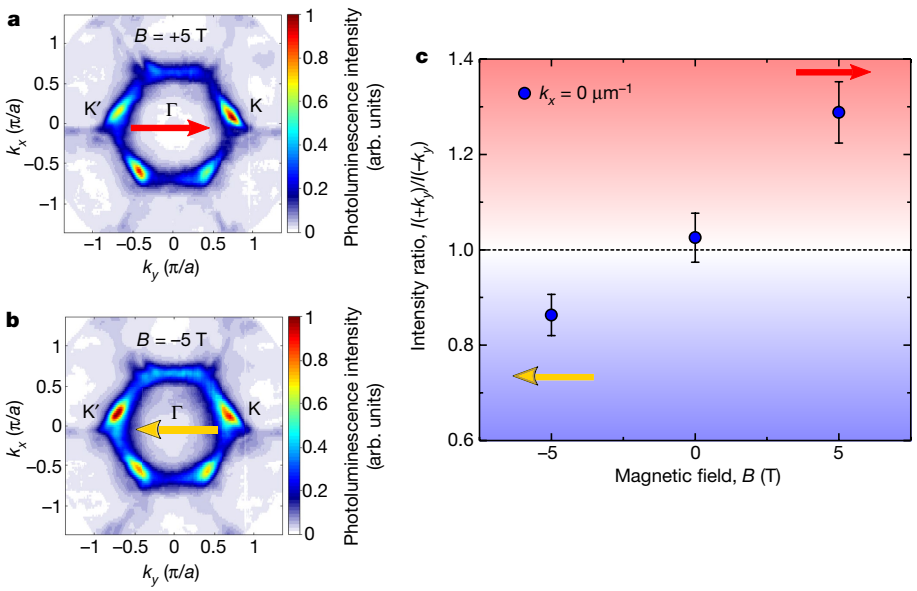

Fig. 4 | Chirality and propagation of the condensate. a, **b**, Spectroscopic hyperspectral measurement of the full *S*-band condensate (1.467–1.468 eV) at the K and K′ points, including the energies linked to the topological edge modes for $B = +5$ T (**a**) and $B = -5$ T (**b**). The zigzag edge is oriented in the *y* direction. **c**, Polariton intensity ratio between the K′ and K points in the k_y direction ($k_x \approx 0$) as a function of the applied magnetic field. The dominant propagation direction is inverted (yellow and red arrows) when the direction of the magnetic field is reversed. For $B = 0$ T, no dominant propagation direction is observed. The error bars originate from image distortions, inhomogeneities of the excitation and uncertainties during data processing, and are estimated at 5%.

curve of the topological edge mode, which is physically manifested in reversing the group velocity. On the other hand, we find no systematic directionality for the peaks at $k_x \approx -0.77\pi/a$ in Fig. 4a, b, which implies that these arise solely from the bulk condensate.

The experimental results depicted in Figs. 3, 4 unequivocally prove the observation of an exciton-polariton topological Chern insulator. The application of a magnetic field to the honeycomb lattice opens up a topological bandgap, with topological edge states supporting unidirectional transport whose propagation direction is determined by the field polarity. The lack of scattering from an artificial defect manifests the robustness of the topological edge mode. Furthermore, the observation of the edge mode extending around the corner and at the armchair termination without bulk scattering is a distinct feature of the topological edge mode, highlighting its topological protection against defects and disorder. Our results lead the way to efficient light trapping and topologically protected propagation of coherent exciton-polariton condensates in a well-developed semiconductor platform in which electrical driving can be envisaged[30]. We now aim to explore the topological lasing aspect of these experiments further, by comparing topological edge-mode lasing with lasing from a trivial edge mode in, for example, a Semenoff insulator. Such experiments would also link our exciton-polariton platform to the recently observed topological insulator laser[31,32]. Because of the interacting nature of polaritons, in-depth study of collective bosonic effects in topological insulators can be envisaged. For example, the large nonlinearity displayed by this exciton-polariton topological system can support the observation of solitons in topological insulators, which have been proposed[33,34] but not yet observed in any system. This work is a step towards new topological polaritonic devices with properties and functionalities involving nonlinearity, gain, interactions and coherence.

Online content

Any methods, additional references, Nature Research reporting summaries, source data, statements of data availability and associated accession codes are available at https://doi.org/10.1038/s41586-018-0601-5.

Received: 8 March 2018; Accepted: 13 August 2018;
Published online 8 October 2018.

1. Hasan, M. Z. & Kane, C. L. Colloquium: topological insulators. *Rev. Mod. Phys.* **82**, 3045–3067 (2010).
2. Klitzing, K. v., Dorda, G. & Pepper, M. New method for high-accuracy determination of the fine-structure constant based on quantized Hall resistance. *Phys. Rev. Lett.* **45**, 494–497 (1980).
3. Haldane, F. D. M. Model for a quantum Hall effect without Landau levels: condensed-matter realization of the "parity anomaly". *Phys. Rev. Lett.* **61**, 2015–2018 (1988).
4. Kane, C. L. & Mele, E. J. Quantum spin Hall effect in graphene. *Phys. Rev. Lett.* **95**, 226801 (2005).
5. Bernevig, B. A., Hughes, T. L. & Zhang, S.-C. Quantum spin Hall effect and topological phase transition in HgTe quantum wells. *Science* **314**, 1757–1761 (2006).
6. König, M. et al. Quantum spin Hall insulator state in HgTe quantum wells. *Science* **318**, 766–770 (2007).
7. Haldane, F. D. M. & Raghu, S. Possible realization of directional optical waveguides in photonic crystals with broken time-reversal symmetry. *Phys. Rev. Lett.* **100**, 013904 (2008).
8. Wang, Z., Chong, Y. D., Joannopoulos, J. D. & Soljacić, M. Observation of unidirectional backscattering-immune topological electromagnetic states. *Nature* **461**, 772–775 (2009).
9. Rechtsman, M. C. et al. Photonic Floquet topological insulators. *Nature* **496**, 196–200 (2013).
10. Hafezi, M., Mittal, S., Fan, J., Migdall, A. & Taylor, J. M. Imaging topological edge states in silicon photonics. *Nat. Photon.* **7**, 1001–1005 (2013).
11. Jotzu, G. et al. Experimental realization of the topological Haldane model with ultracold fermions. *Nature* **515**, 237–240 (2014).
12. Aidelsburger, M. et al. Measuring the Chern number of Hofstadter bands with ultracold bosonic atoms. *Nat. Phys.* **11**, 162–166 (2015).
13. Yang, Z. et al. Topological acoustics. *Phys. Rev. Lett.* **114**, 114301 (2015).
14. Fleury, R., Khanikaev, A. B. & Alù, A. Floquet topological insulators for sound. *Nat. Commun.* **7**, 11744 (2016).
15. Süsstrunk, R. & Huber, S. D. Observation of phononic helical edge states in a mechanical topological insulator. *Science* **349**, 47–50 (2015).
16. Karzig, T., Bardyn, C.-E., Lindner, N. H. & Refael, G. Topological polaritons. *Phys. Rev. X* **5**, 031001 (2015).
17. Bardyn, C.-E., Karzig, T., Refael, G. & Liew, T. C. H. Topological polaritons and excitons in garden-variety systems. *Phys. Rev. B* **91**, 161413(R) (2015).
18. Nalitov, A. V., Solnyshkov, D. D. & Malpuech, G. Polariton $\mathbb{Z}$ topological insulator. *Phys. Rev. Lett.* **114**, 116401 (2015).
19. Weisbuch, C., Nishioka, M., Ishikawa, A. & Arakawa, Y. Observation of the coupled exciton-photon mode splitting in a semiconductor quantum microcavity. *Phys. Rev. Lett.* **69**, 3314–3317 (1992).
20. Kasprzak, J. et al. Bose–Einstein condensation of exciton polaritons. *Nature* **443**, 409–414 (2006).
21. Carusotto, I. & Ciuti, C. Quantum fluids of light. *Rev. Mod. Phys.* **85**, 299–366 (2013).
22. Schneider, C. et al. Exciton-polariton trapping and potential landscape engineering. *Rep. Prog. Phys.* **80**, 016503 (2017).
23. St-Jean, P. et al. Lasing in topological edge states of a one-dimensional lattice. *Nat. Photon.* **11**, 651–656 (2017).
24. Peleg, O. et al. Conical diffraction and gap solitons in honeycomb photonic lattices. *Phys. Rev. Lett.* **98**, 103901 (2007).
25. Jacqmin, T. et al. Direct observation of Dirac cones and a flatband in a honeycomb lattice for polaritons. *Phys. Rev. Lett.* **112**, 116402 (2014).
26. Milićević, M. et al. Edge states in polariton honeycomb lattices. *2D Mater.* **2**, 034012 (2015).
27. Fujita, M., Wakabayashi, K., Nakada, K. & Kusakabe, K. Peculiar localized state at zigzag graphite edge. *J. Phys. Soc. Jpn* **65**, 1920–1923 (1996).
28. Castro Neto, A. H., Guinea, F., Peres, N. M. R., Novoselov, K. S. & Geim, A. K. The electronic properties of graphene. *Rev. Mod. Phys.* **81**, 109–162 (2009).
29. Yao, Y., Ye, F., Qi, X.-L., Zhang, S.-C., and Fang, Z. Spin–orbit gap of graphene: first-principles calculations. *Phys. Rev. B* **75**, 041401(R) (2007).
30. Suchomel, H. et al. A plug and play platform for electrically pumped polariton simulators and topological lasers. Preprint at https://arxiv.org/abs/1803.08306 (2018).
31. Bahari, B. et al. Nonreciprocal lasing in topological cavities of arbitrary geometries. *Science* **358**, 636–640 (2017).
32. Bandres, M. A. et al. Topological insulator laser part II: experiments. *Science* **359**, aar4005 (2018).
33. Lumer, Y., Plotnik, Y., Rechtsman, M. C. & Segev, M. Self-localized states in photonic topological insulators. *Phys. Rev. Lett.* **111**, 243905 (2013).
34. Kartashov, Y. V. & Skryabin, D. V. Modulational instability and solitary waves in polariton topological insulators. *Optica* **3**, 1228–1236 (2016).

Acknowledgements We thank R. Thomale for discussions. S.K. acknowledges the European Commission for the H2020 Marie Skłodowska-Curie Actions (MSCA) fellowship (Topopolis). S.K., S.H. and M.S. are grateful for financial support by the JMU-Technion seed money programme. S.H. also acknowledges support by the EPSRC "Hybrid Polaritonics" grant (EP/M025330/1). The Würzburg group acknowledges support by the ImPACT Program, Japan Science and Technology Agency and the ENB programme (Tols 836315) of the State of Bavaria. T.C.H.L. and R.G. were supported by the Ministry of Education (Singapore) grant no. 2017-T2-1-001.

Author contributions S.K., M.S., C.S. and S.H. initiated the study and guided the work. S.K., T.H., K.W., M.E. and S.H. designed and fabricated the device. S.K. and T.H. performed optical measurements. S.K., T.H., O.A.E. and C.S. analysed and interpreted the experimental data. O.A.E., R.G., T.C.H.L., M.A.B. and M.S. developed the theory. S.K., T.H., O.A.E., T.C.H.L., C.S., M.S. and S.H. wrote the manuscript, with input from all co-authors.

Competing interests The authors declare no competing interests.

Additional information
Extended data is available for this paper at https://doi.org/10.1038/s41586-018-0601-5.
Reprints and permissions information is available at http://www.nature.com/reprints.
Correspondence and requests for materials should be addressed to S.K. or S.H.
Publisher's note: Springer Nature remains neutral with regard to jurisdictional claims in published maps and institutional affiliations.

METHODS

Basic sample characterization. Honeycomb lattices of coupled micropillars were etched into a planar semiconductor Fabry–Pérot microcavity, grown by molecular beam epitaxy. The cavity consists of a GaAs λ-cavity equipped with three 16-nm-wide $In_{0.04}Ga_{0.96}As$ quantum wells sandwiched between two distributed Bragg reflectors with 30 (35.5) $Al_{0.10}Ga_{0.90}As$/AlAs top (bottom) mirror pairs. The quantum wells were placed at the maximum of the electromagnetic field, resulting in a strong exciton-photon coupling with a Rabi splitting of 4.3 meV (see Extended Data Fig. 1). The set of quantum wells emit with an exciton linewidth of $\gamma_X = 1.2$ meV (full width at half maximum), measured with the top mirror etched away. The quality factor of the cavity was determined experimentally by measuring the mode linewidth of a single large pillar at a negative (photonic) detuning, $\delta \approx -11.5$ meV, to be about 13.000 ($\gamma_C = 0.11$ meV). The overall layer thicknesses decrease radially towards the outside of the wafer, affecting mainly the photonic mode. The decrease in thickness allows the experimenter to choose a certain exciton-to-photon detuning. By increasing the asymmetry between the cavity mode and the stopband centre, the TE–TM splitting of the cavity mode is increased, mimicking a spin–orbit interaction[35]. However, the further the cavity mode is moved towards the edge of the stopband, the lower the reflectivity becomes, implying a lower Q-factor and larger polariton linewidth. Based on simulations and experience from previously grown samples, a DBR (cavity) asymmetry factor of 1.03 (0.91) was chosen for the microcavities presented in this work (1.00 (1.00) would be the symmetric case), yielding a TE–TM splitting of approximately 600 μeV at $k_\parallel = 2.0\,\mu m^{-1}$ (see Extended Data Fig. 2). Both the indium content in the InGaAs quantum well and the quantum-well thickness were optimized with regards to the smallest linewidth and largest Zeeman splitting. 4% indium and 16 nm thickness yield a Zeeman splitting $\Delta E_Z = 540$ μeV at $B = 5$ T (see Extended Data Fig. 2). After sample growth, a honeycomb lattice of approximately $(120 \times 120)\,\mu m^2$ with a pillar diameter of $d = 2.0\,\mu m$ and an overlap $v = a/d = 0.85$ was defined using an electron beam lithography process and subsequent wet etching. Extended Data Fig. 3 shows a microscope image of an intended defect in the form of a site missing in a zigzag edge of the honeycomb lattice (indicated by the red arrow).

Photoluminescence experiment. Non-resonant photoluminescence experiments with and without an applied magnetic field were carried out using a linearly polarized, pulsed titanium-sapphire laser with a repetition rate of 82 MHz and a pulse length of approximately 2 ps. The wavelength of the laser was set to be $\lambda_L = 792$ nm, coinciding with the first high-energy stopband minimum of the microcavity structure.

The emission was collected using a microscope objective (20×, NA = 0.4) and imaged at the entrance slit of a Czerny–Turner spectrometer, equipped with a charge-coupled device (CCD) camera with a resolution of about 20 μeV. A motorized imaging lens allows for automated hyperspectral images ((k_x, k_y) versus E) and mode tomographies ((x, y) versus E).

The sample was mounted in a liquid helium flow cryostat (Oxford Instruments Microstat), operating at a temperature of $T = 4$ K. Using superconducting coils, a magnetic field $B = -5$ T to $+5$ T can be applied in Faraday geometry.

Bloch-mode calculations for polariton honeycomb lattices. A widely accepted model describes the dynamics of excitons with spin-up (ψ^+) and spin-down (ψ^-) coupled to cavity photons carrying the right (E^+) and the left (E^-) circular polarizations, respectively[18,34,36], and is governed by

$$i\hbar\partial_t E^\pm = \left(-\frac{\hbar^2}{2m_C}\nabla_\perp^2 + V(\boldsymbol{r}) + \omega_C - i\gamma\right)E^\pm + \beta(\partial_x \mp i\partial_y)^2 E^\mp + \hbar\Omega_R\psi^\pm + E_p^\pm e^{-i\omega_p t} \quad (1)$$

$$i\hbar\partial_t \psi^\pm = \left(\omega_E - i\gamma \pm \frac{\Delta_B}{2}\right)\psi^\pm + \hbar\Omega_R E^\pm \quad (2)$$

(where ∂_t represents partial derivative with respect to time t, and E_p is the external coherent radiation explained below). Here, the normalization is such that $|E^\pm|^2$ and $|\psi^\pm|^2$ are the number of particles per unit area. The quantities ω_C and ω_E represent the energies of bare photons and excitons, respectively. In the present configuration, the photon–exciton detuning is negative, $\delta = (\omega_C - \omega_E) = -6$ meV. The photon–exciton coupling strength is given by the parameter $\hbar\Omega_R$, which defines the Rabi splitting as $2\hbar\Omega_R = 4.5$ meV. Here, $m_C = 32.3 \times 10^{-6} m_e$ is the effective photon mass in the planar region, and m_e is the free electron mass. The effective mass of excitons is $m_E \approx 10^5 m_C$. An external photonic potential $V(\boldsymbol{r})$ is defined within the unit cell of the honeycomb structure, constructed of circular mesas (micropillars). We assume that the potential is $V(\boldsymbol{r}) = 30$ meV outside the mesas and zero otherwise. In what follows, we assume that the intensity of polaritons is weak enough and thus neglect nonlinear interactions between them. The TE–TM splitting of the cavity modes gives rise to the linear coupling between right- and left- circular polarizations and is denoted by β (ref. [36]). We account for the magnetic field via Zeeman splitting Δ_B of the excitonic states in the quantum wells.

Equations (1) and (2) allow for accurate simulation of the propagation of the chiral modes coherently injected into the system by means of the external coherent radiation ($E_p^\pm$), with an appropriately chosen frequency (ω_p) within the topological gap. First, we calculate the energy–momentum band structure of the honeycomb lattices, using a full description of the Bloch modes that takes into account all relevant system parameters. For this aim, we solve the following eigenvalue problem for the energy $\hbar\mu(\boldsymbol{k}_b)$ of the Bloch mode with the Bloch vector $\boldsymbol{k}_b = (k_{bx}, k_{by})$

$$\hbar\mu(\boldsymbol{k}_b)\begin{pmatrix}\boldsymbol{p}_b^+(\boldsymbol{r},\boldsymbol{k}_b)\\ \boldsymbol{p}_b^-(\boldsymbol{r},\boldsymbol{k}_b)\end{pmatrix} = \begin{pmatrix}\hat{L}^+ & \hat{C}^+\\ \hat{C}^- & \hat{L}^-\end{pmatrix}\begin{pmatrix}\boldsymbol{p}_b^+(\boldsymbol{r},\boldsymbol{k}_b)\\ \boldsymbol{p}_b^-(\boldsymbol{r},\boldsymbol{k}_b)\end{pmatrix} \quad (3)$$

The circularly polarized polaritonic wavefunctions are $\boldsymbol{p}_b^\pm(\boldsymbol{r},\boldsymbol{k}_b) = (c_b^\pm(\boldsymbol{r},\boldsymbol{k}_b), x_b^\pm(\boldsymbol{r},\boldsymbol{k}_b))$, where the functions $c_b^\pm(\boldsymbol{r},\boldsymbol{k}_b)$ and $x_b^\pm(\boldsymbol{r},\boldsymbol{k}_b)$ describe the amplitude distributions of the photonic and excitonic component of the Bloch modes in real space, defined in the plane of the microcavity $\boldsymbol{r} = (x, y)$. The diagonal of the matrix in equation (3) describes the single-particle coupled states of excitons and photons and is given by the expression

$$\hat{L}^\pm = \begin{pmatrix}\omega_C + V(\boldsymbol{r}) - \frac{\hbar^2}{2m_C}(\nabla_\perp + i\boldsymbol{k}_b)^2 & \hbar\Omega_R\\ \hbar\Omega_R & \omega_E - \frac{\hbar^2}{2m_E}(\nabla_\perp + i\boldsymbol{k}_b)^2 \pm \frac{\Delta_B}{2}\end{pmatrix} \quad (4)$$

The coupling between both polarization components is given by the matrices $\hat{C}^\pm$

$$\hat{C}^\pm = \begin{pmatrix}\beta[(\nabla_\perp + i\boldsymbol{k}_b)\cdot(\boldsymbol{e}_x \mp i\boldsymbol{e}_y)]^2 & 0\\ 0 & 0\end{pmatrix} \quad (5)$$

which includes the TE–TM splitting of the photonic modes. Δ_B describes the Zeeman splitting of the excitons due to the applied magnetic field. The unit vectors $\boldsymbol{e}_{x,y}$ shows the directions of Cartesian coordinates (x, y) in the plane of the microcavity. To reduce computational efforts greatly, it is convenient to solve the eigenvalue problem in polaritonic basis after diagonalization of the matrix $\hat{L}^\pm$, describing the coupling between photons and excitons. In this case, the effective parameter for the TE–TM splitting $\beta_{eff} \approx \beta|C|^2$ and the Zeeman splitting $\Delta_{eff} \approx \Delta_B|X|^2$ are scaled with the photonic and excitonic components of the polaritons, respectively (where $|C|^2$ and $|X|^2$ are the Hopfield coefficients, calculated for the respective Bloch mode).

Physically, the excitation occurs by coherent illumination with linearly polarized light at the frequency within the topological gap. The seeding pulse duration is about 40 ps. Other parameters: $\Delta_B = \pm 0.8$ meV, $\beta = 0.20$ meV μm^2, $\beta_{eff} = 0.15$ meV μm^2, $\gamma = 0.01$ meV, polariton lifetime $\tau = 35$ ps, pillar diameter $d = 2.0\,\mu m$, centre-to-centre separations $a = 2\,\mu m$.

Polariton chiral edge mode propagating around a corner and defect. Using the Bloch mode calculations described above, we now excite the system resonantly and calculate its evolution in time for a Zeeman splitting of $\Delta_B = +0.8$ meV. The polaritons propagate along the edge and around the 90° corner as expected for a topological edge mode (see Extended Data Fig. 4). In the same way, we find that the edge mode avoids an artificial defect in the form of a site missing in a zigzag chain (see Extended Data Fig. 5).

Tight-binding model. A tight-binding model describing the artificial graphene band structure is given by

$$E_{hc}(\boldsymbol{k}_\parallel) = E_0 \pm t\sqrt{3 + f(\boldsymbol{k}_\parallel)} - t' f(\boldsymbol{k}_\parallel) \quad (6)$$

$$f(\boldsymbol{k}_\parallel) = 2\cos(\sqrt{3}k_y a) + 4\cos\left(\frac{\sqrt{3}}{2}k_y a\right)\cos\left(\frac{3}{2}k_x a\right) \quad (7)$$

Here, t is the nearest neighbour, t' is the next-nearest neighbour and $\boldsymbol{k}_\parallel$ is the measured in-plane lattice vector, which is linked to the measured polariton emission angle θ by $k_\parallel = (\omega/c)\sin\theta$. The resulting band structure of this model is presented as a fit to the data in Fig. 2f, in red and yellow-brown.

Gap measurement. When an external magnetic field is applied to this lattice, a bandgap is predicted to open at the Dirac points. We make use of a $\lambda/4$ polarization series to detect this gap. In Extended Data Fig. 6, exemplary images of the $\lambda/4$-series at external magnetic fields of $B = 0$ T and 5 T are presented. The energetic position of the Dirac point was evaluated by fitting a Lorentzian peak profile to the line spectrum through the Dirac point at K′. The peak positions were plotted against the angle of the $\lambda/4$-waveplate. Assuming that the position of

the peak corresponds linearly to its polarization, the resulting graph can be fitted using the equation

$$I(\phi) = \frac{1}{2}[S_0 + S_1\cos^2(2\phi) + S_2\sin(2\phi)\cos(2\phi) + S_3\sin(2\phi)]$$

normally used to fit the peak intensity in a $\lambda/4$-series with a constant peak position. At $B = +5$ T, a bandgap of $E_g = 108 \pm 32\,\mu$eV was evaluated. The peak movement with no external magnetic field applied can be attributed to imperfections of the $\lambda/4$-waveplate. It was used to indicate the uncertainty of the bandgap that opens when an external magnetic field is applied.

Input/output characteristics and linewidth. By increasing the power of the non-resonant pump laser, measuring the intensity and linewidth we determine the threshold characteristic of the polaritons as shown in Extended Data Fig. 7. At a typical threshold of $P_{th} \approx 1.8$ mW a distinct nonlinear increase in intensity as well as a sudden decrease in linewidth can be observed. The mode associated with the gap mode becomes visible around $P = P_{th}$.

Ginzburg–Landau calculations of polariton condensation into a topological edge mode. In theoretical proposals such as in refs [16–18], no particular form of excitation was considered explicitly. It is clear from the theoretical Bloch mode calculations that a resonant excitation is able to directly populate the various modes. For the case of non-resonant excitation, further theoretical work is needed to access the physics of polariton condensation into a chiral topological edge mode, described in Fig. 3.

Here we use the driven-dissipative Ginzburg–Landau model, frequently used to describe the spatial form of polariton condensates:

$$i\hbar\frac{\partial}{\partial t}\begin{pmatrix}\psi_+\\ \psi_-\end{pmatrix} = \begin{pmatrix}\hat{L}_0 + \frac{\Delta_{\text{eff}}}{2} - i|\psi_+|^2 & \beta_{\text{eff}}(\hat{k}_x - i\hat{k}_y)^2\\ \beta_{\text{eff}}(\hat{k}_x + i\hat{k}_y)^2 & \hat{L}_0 - \frac{\Delta_{\text{eff}}}{2} - i|\psi_-|^2\end{pmatrix}\begin{pmatrix}\psi_+\\ \psi_-\end{pmatrix} \quad (8)$$

Here ψ_+ and ψ_- denote the two spin components of the two-dimensional polariton wavefunction. The operator $\hat{L}_0$ is defined as $\hat{L}_0 = \hat{E}_0 + V(\boldsymbol{r}) + iW(\boldsymbol{r})$, where the operator $\hat{E}_0$ corresponds to the bare kinetic energy of polaritons, modelled with an effective mass m. The potential $V(\boldsymbol{r})$ accounts for the honeycomb lattice structure and Δ_{eff} is the Zeeman splitting caused by the applied magnetic field. The two spin components are coupled by the off-diagonal spin–orbit coupling term, physically corresponding to a TE–TM splitting with strength β_{eff}.

The linear gain and loss in the system is described by the term $W(\boldsymbol{r}) = P(\boldsymbol{r}) - \Gamma(\boldsymbol{r})$, where $P(\boldsymbol{r})$ represents the spatially dependent non-resonant pumping and $\Gamma(\boldsymbol{r})$ is a spatially dependent dissipation rate. We assume that the loss is higher outside the micropillar regions. For the system to form a steady state, it is important to consider also nonlinear loss terms. For simplicity, we neglect the effect of polariton–polariton interactions, which is valid provided we operate not too far above the condensation threshold.

Before solving the full nonlinear problem, it is instructive to consider the spectrum of linearized modes, obtained by neglecting the nonlinear term. Considering a strip geometry, where the potential is periodic in the x direction and bounded in the orthogonal y direction, the Bloch theory can be used to obtain the complex band structure of the system eigenmodes with respect to a wavevector k_x. The result is shown in Extended Data Fig. 8a. For parameters comparable with the experiment, we obtain a topological bandgap bridged by chiral edge states. A slight asymmetry in the edge states occurs owing to the pumping $P(\boldsymbol{r})$, which is taken to be periodic in the x direction (to maintain validity of the Bloch theory) but preferentially localized near the bottom edge of the strip.

Extended Data Fig. 8b shows the imaginary parts of the same eigenmodes. The chiral edge state is found to have the largest imaginary component, meaning that it has a larger gain than other states and would be preferentially selected during polariton condensation. However, it should be noted that in principle there are an infinite number of energy states obtainable with the present theory, and it is necessary in practice to introduce an energy cut-off to solve the Bloch Hamiltonian.

To rule out the potential population of higher energy states, we rely on solution of the full nonlinear problem, propagating equation (8) in time to a steady state. Here we do indeed find condensation in a chiral edge state, as illustrated with the colour scale in Extended Data Fig. 8a. A slight shift from the results of the linear band-structure calculation occurs because of the nonlinear term. Extended Data Fig. 8c shows the obtained wavefunction in real space, which is indeed localized at the edge excited by the pumping, agreeing with the experimental findings. In addition to explaining our experimental observation of chiral current under non-resonant pumping, these theoretical results predict a polariton lasing in a topological edge state: a topological polariton laser[31,32]. However, we point out that a strict comparison between a topological laser and a non-topological laser (as in ref. [32]) cannot easily be made, as the topological gap cannot be closed without changing a wide range of other system parameters.

Real-space mode tomographies at $B = 0$ T and $B = -5$ T. For the sake of completeness, we perform the same mode tomographies at $B = 0$ T and $B = -5$ T as were displayed in Fig. 3 for $B = +5$ T. The results are displayed in Extended Data Fig. 9a–d ($B = 0$ T) and Extended Data Fig. 9e–h ($B = -5$ T). Whereas for the $B = 0$ T case no distinct edge mode is observed, the behaviour for $B = -5$ T is qualitatively similar to that for $B = +5$ T, as expected.

Data availability

The research data that support this publication can be accessed at https://doi.org/10.17630/4a62cbdd-bcae-45d7-a556-3cda53c0a656. Additional data related to this paper may be requested from the corresponding authors.

35. Sala, V. G. et al. Spin–orbit coupling for photons and polaritons in microstructures. *Phys. Rev. X* **5**, 011034 (2015).
36. Deveaud, B. *The Physics of Semiconductor Microcavities* (Wiley-VCH, Weinheim, 2007).

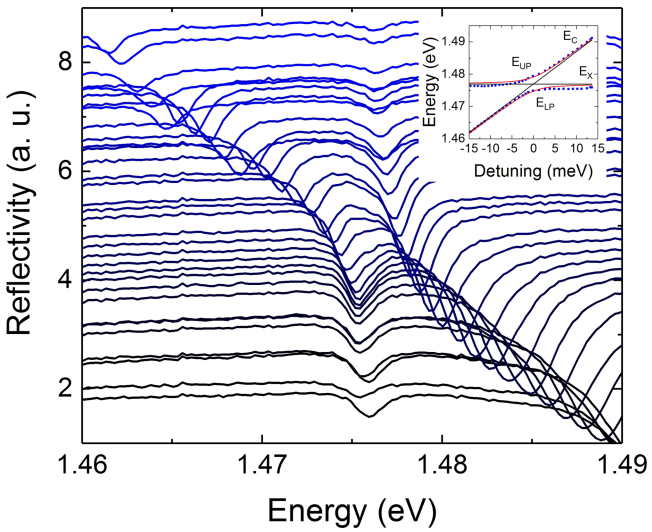

Extended Data Fig. 1 | White-light reflectivity measurements as a function of the detuning. Reflectivity measurements are shown as a function of the detuning. A distinct anticrossing behaviour with a Rabi splitting of $2\hbar\Omega_R = 4.3$ meV can be observed. The measurements were performed on a sample piece with approximately 15 mirror pairs removed from the top DBR to increase the signal quality. Inset, fitted peak positions versus detuning. UP and LP stand for upper polariton and lower polariton.

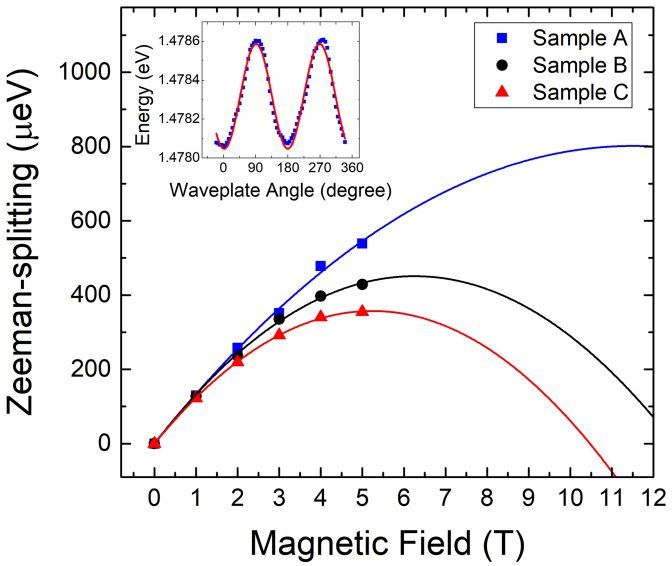

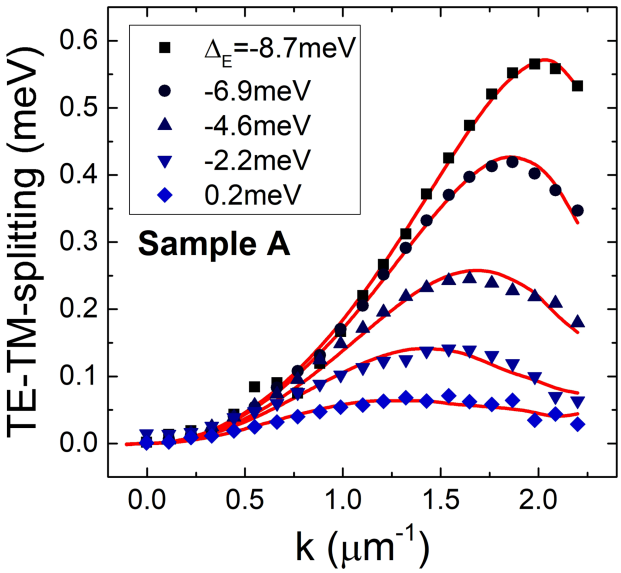

Extended Data Fig. 2 | Zeeman splitting and TE–TM splitting for a III–V microcavity hosting $In_{0.04}Ga_{0.96}As$ quantum wells. Left, Zeeman splitting with regard to the magnetic field, including second-order polynomial fits as a guide to the eye. Sample A is the one used in this experiment. Inset, example of central emission energies for a $\lambda/4$-series with a sine fit. Right, experimentally determined TE–TM splitting at various detunings Δ_E for sample A including fits with modified photonic Hopfield coefficients (red).

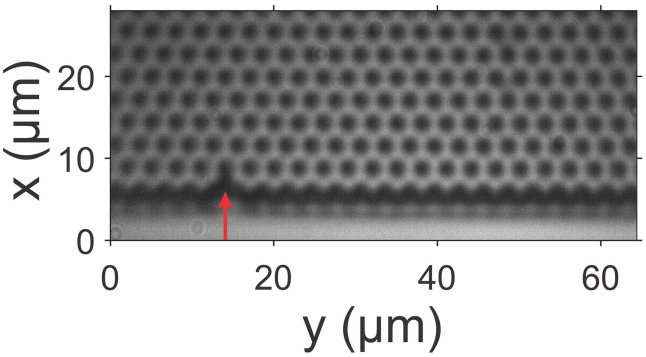

Extended Data Fig. 3 | Microscopy image of a zigzag-edge polariton honeycomb lattice with an intentional defect. Shown is an image of the honeycomb lattice with $d = 2.0\,\mu m$ and $v = 0.85$, with an intentional defect in the zigzag chain, selected for experiments in an external magnetic field.

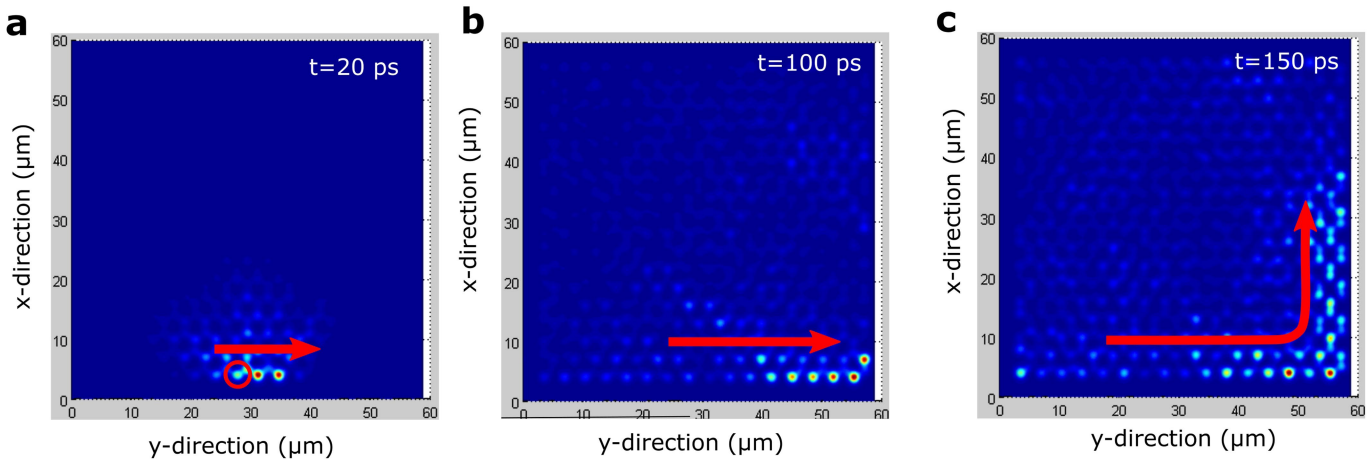

Extended Data Fig. 4 | Polariton chiral edge mode propagating around a corner. a–c, Propagation dynamics of edge modes injected coherently into the topological gap and calculated within model 1. Shown here is the right-moving propagation for the positive-value splitting $\Delta_B = +0.8$ meV ($|\Delta_{eff}| = 0.2$ meV) and $\beta = 0.20$ meV μm^2 ($\beta_{eff} = 0.15$ meV μm^2). A linearly polarized narrow coherent seeding beam injects both polarization components into the region marked by the red circle. At $t \approx 100$ ps, the mode propagates around the corner from the zigzag edge into the armchair one.

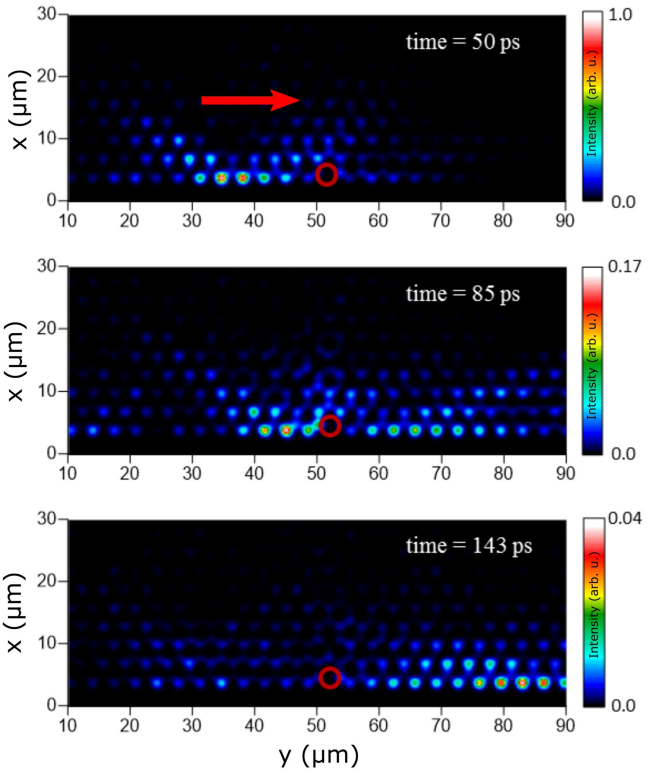

Extended Data Fig. 5 | Polariton chiral edge mode propagating and avoiding a defect. Propagation dynamics of edge modes injected coherently into the topological gap and calculated within model 1 are shown for the right-moving propagation for the positive-value splitting $\Delta_B = +0.8$ meV ($|\Delta_{eff}| = 0.2$ meV) and $\beta = 0.20$ meV μm^2 ($\beta_{eff} = 0.15$ meV μm^2). A linearly polarized narrow coherent seeding beam injects both polarization components into the mesa. At $t \approx 85$ ps, the mode propagates around the defect in the zigzag chain, marked by the red circle.

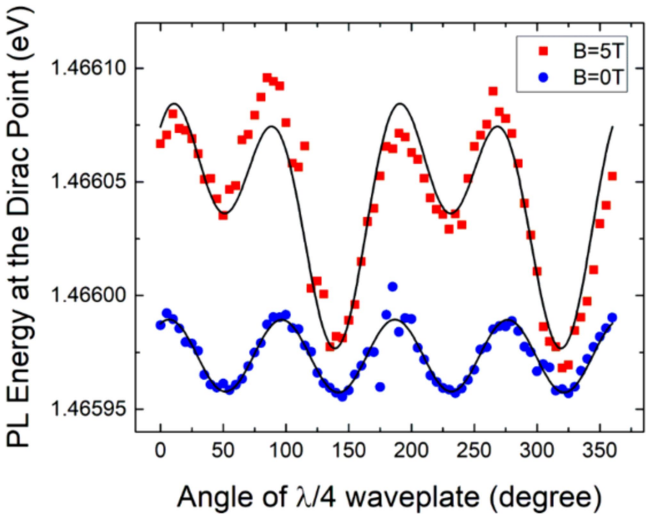

Extended Data Fig. 6 | Topological gap measurement. A $\lambda/4$-plate measurement at $B = 0$ T (blue) and $B = +5$ T (red) at the K point yields a bandgap of $E_g = 108 \pm 32\,\mu$eV. PL, photoluminescence.

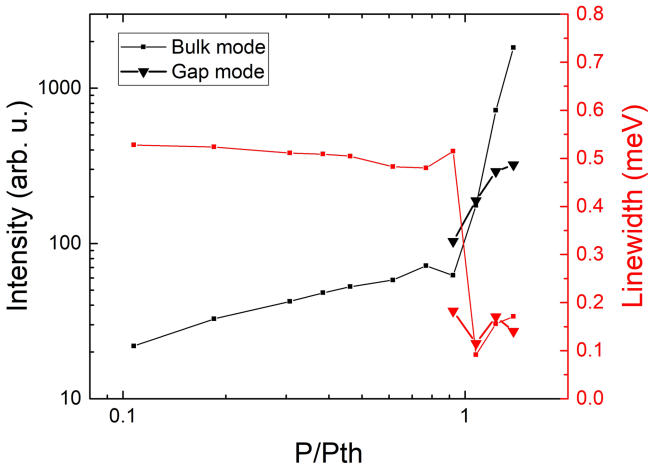

Extended Data Fig. 7 | Input/output characteristics and linewidth behaviour as a function of pump power. Below threshold, the gap and bulk mode cannot be distinguished. At a typical threshold $P_{th} \approx 1.8$ mW, a distinct nonlinear increase in intensity as well as a sudden decrease in linewidth can be observed. Here, the populated gap modes show similar behaviour to the bulk mode.

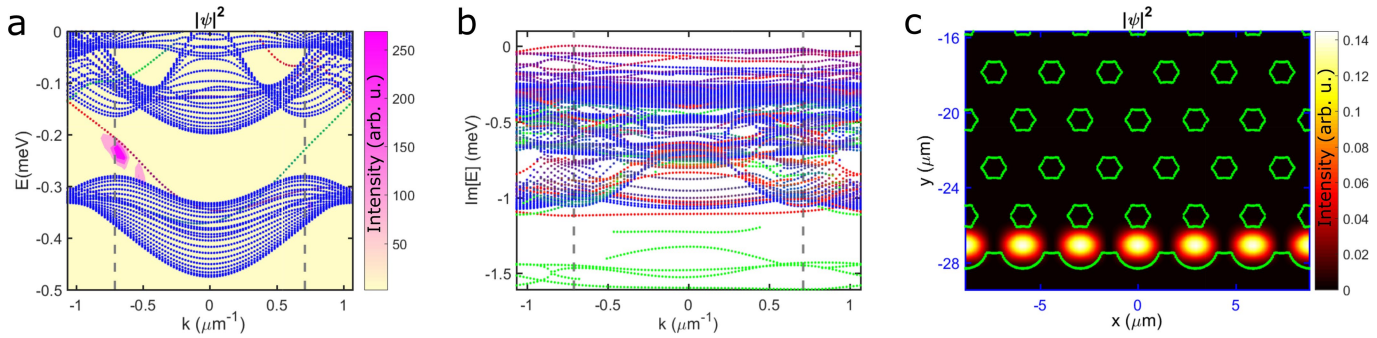

Extended Data Fig. 8 | Driven-dissipative Gross–Pitaevskii calculation of polariton condensation into topological edge mode. a, Band structure of polaritons in a honeycomb lattice. The dotted curves represent the dispersion of the linear eigenmodes of a strip, colour-coded to represent localization on the bottom edge (red), upper edge (green) and in the bulk (blue). The shaded region represents the energy and momentum of the polariton steady state obtained from solving the driven-dissipative Gross–Pitaevskii equation. **b**, Imaginary components of the linear eigenmodes. The largest imaginary part corresponds to an edge state (the colour coding is the same as in **a**), suggesting that the edge state is most likely to be populated with increasing pumping. **c**, Edge state obtained from solution of the driven-dissipative Gross–Pitaevskii equation. Parameters: $\Delta_{\mathrm{eff}} = 0.3$ meV, $\beta_{\mathrm{eff}} = 0.2$ meV μm^2. The effective mass m was taken as 1.3×10^{-4} of the free electron mass; the potential of depth 0.5 meV was constructed from a honeycomb lattice of cylinders of radius 1 μm and centre-to-centre separation 1.7 μm; the pump spot was taken as a Gaussian centred on the strip edge with extent 7.5 μm in the y direction. A spatially uniform decay rate of 0.2 meV was supplemented with a 1.7 meV decay in the region outside the cylinders.

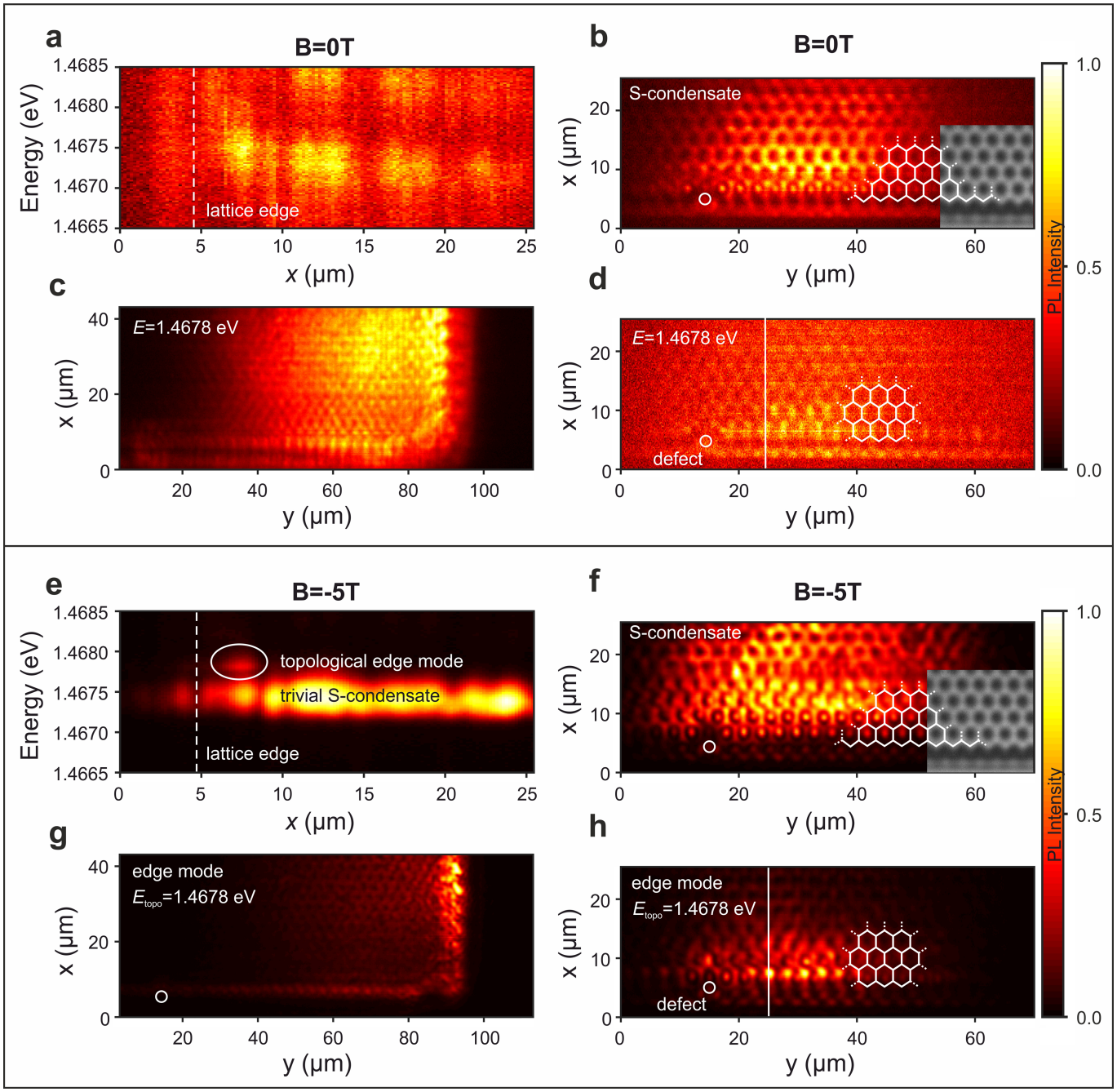

Extended Data Fig. 9 | Real-space mode tomographies of a polariton condensate at $B = 0$ T and $B = -5$ T. a–d, Measurements at $B = 0$ T. **a**, Real-space spectrum in x direction perpendicular to the zigzag edge along the straight white line in **d**. The real-space x axis is consistent between **a**, **b** and **d**. The dashed white line marks the physical edge of the lattice. Only a trivial S-band condensate can be observed throughout the structure. **b**, Mode tomography displaying the topologically trivial S-band condensate at $E_S = 1.4673$–1.4675 eV. A relatively homogeneous condensate within the pump spot diameter of 40 μm is observed. The inset shows a microscopy image of the structure. **c**, **d**, Mode tomography of the energy $E_{edge} = 1.4678$ eV for comparison at the corner position (**c**) and at the edge (**d**) of the sample. Without magnetic field, no localized edge mode can be observed. **e**–**h**, Measurements at $B = -5$ T (fully analogous to Fig. 3d–g). **e**, Real-space spectrum in the x direction perpendicular to the zigzag edge along the straight white line in **h**. The real-space x axis is consistent between **e**, **f** and **h**. The dashed white line marks the physical edge of the lattice. A trivial S-band condensate can be observed throughout the structure. At $E = 1.4678$ eV, again we observe the appearance of a localized mode, well separated from the bulk and located at the zigzag edge. **f**, Mode tomography displaying the topologically trivial S-band condensate at $E_S = 1.4673$–1.4675 eV. A relatively homogeneous condensate within the pump spot diameter of 40 μm is observed. The inset shows a microscopy image of the structure. **g**, **h**, Mode tomography of the topological edge mode at $E_{edge} = 1.4678$ eV at the corner position (**g**) and at the edge (**h**) of the sample, showing clearly that the mode extends around the corner from the zigzag to the armchair configuration and avoids the intentional defect, both without bulk scattering.